Construction and Building Materials 66 (2014) 731–742

Contents lists available at ScienceDirect

Construction and Building Materials

journal homepage: www.elsevier.com/locate/conbuildmat

Microstructure-informed modelling of damage evolution in cement paste

Mingzhong Zhang, Andrey P. Jivkov *

Mechanics and Physics of Solids Research Team, School of Mechanical, Aerospace and Civil Engineering, The University of Manchester, Oxford Road, Manchester M13 9PL, UK

HIGHLIGHTS

- Macroscopic behaviour from microstructure features and meso-scale principles.
- Derivation of microstructure features from high-resolution micro-CT images.
- Construction of site-bond model with microstructure information.
- Demonstration of agreement between calculated responses and experimental data.
- Quantitative assessment of microstructure effects on macroscopic behaviour.

ARTICLE INFO

Article history:
Received 27 January 2014
Received in revised form 6 May 2014
Accepted 12 June 2014

Keywords:
Cement paste
Microstructure
Image analysis
Micromechanics
Brittle ligament
Damage evolution

ABSTRACT

Cement paste is a binder for cementitious materials and plays a critical role in their engineering-scale properties. Understanding fracture processes in such materials requires knowledge of damage evolution in cement paste. A site-bond model with elastic-brittle spring bundles is developed here for analysis of the mechanical behaviour of cement paste. It incorporates key microstructure information obtained from high resolution micro-CT. Volume fraction and size distribution of anhydrous cement grains are used for calculating model length scale and elasticity. Porosity and pore size distribution are used to allocate local failure energies. Macroscopic damage emerges from the generation of micro-crack population represented by bond removals. Effects of spatial distribution, porosity and sizes of pores on tensile strength and damage are investigated quantitatively. Results show a good agreement with experiment data, demonstrating that the proposed technology can predict mechanical and fracture behaviour of cementitious materials based exclusively on microstructure information.

1. Introduction

Concrete is the most popular and widely used construction material in the world. The fracture behaviour of concrete has been a great concern for many years and remains a challenge due to concrete's complex and heterogeneous porous microstructure extending over wide range of length scales from nanometres to millimetres [1]. At meso-scale, concrete can be considered as a three-phase composite consisting of aggregate, matrix (i.e. cement paste) and interfacial transition zone (ITZ) between aggregate and matrix. ITZ is a "special" cement paste that has a higher initial water-to-cement mass ratio (w/c) compared to matrix [2]. Therefore, to study the mechanical properties and failure of concrete, one must first understand the damage evolution and fracture process in cement paste, which depends on its microstructure.

In order to characterise the 3D microstructure of cement paste, a variety of techniques including computer-aided simulation and experimental tests have been proposed and developed in the past few decades. Among them, computer-based cement hydration models, e.g. CEMHYD3D [3], HYMOSTRUC3D [4,5] and the more recently proposed μic (pronounced Mike) [6] are commonly applied to simulate the hydration process and gradual formation of the microstructure of cement paste. As a non-destructive technique, X-ray micro-computed tomography (micro-CT) has many advantages compared to other experimental techniques and has been successfully utilised to obtain the 3D microstructure of cement paste at a high resolution of 0.5 μm/voxel [7].

Many approaches have been proposed to develop the so-call micromechanical models by taking into account the underlying microstructure and mechanical properties of components of cement paste in recent years [8–20]. The important feature of the micromechanical models is that the material damage at the continuous level is introduced by the nucleation and evolution of micro-

* Corresponding author. Tel.: +44 161 306 3765.
E-mail address: andrey.jivkov@manchester.ac.uk (A.P. Jivkov).

http://dx.doi.org/10.1016/j.conbuildmat.2014.06.017
0950-0618/

cracks. Discrete lattice models that represent a material by a lattice system of beam or spring elements are the most popular micromechanical models and seem to offer promising modelling strategy to explain fracture processes in cement paste [20]. Based on the simplest regular lattice with cubic cells, a lattice beam model has been proposed by Schlangen and van Mier [8], and further developed and adopted by Qian [19] to simulate the fracture processes in cementitious materials at different length scales. However, it has been pointed out that this lattice is not physically realistic in terms of shape of the represented phases in cement paste and is unable to provide a linear elastic response with an appropriate elastic modulus and Poisson's ratio [21]. Moreover, the obtained stress–strain curves of cement paste under uniaxial tests remain not realistic [14]. Man [15] developed two more complex 3D lattice beam models based on face-centred cubic packing (fcc) and hexagonal close packing (hcp) to investigate the fracture behaviour of concrete at meso-scale. However, the effects of spatial and size distribution of pores were not taken into account.

To overcome such limitations a site-bond model using a bi-regular lattice of truncated octahedral cells for elasticity has been recently proposed by Jivkov and Yates [21] and subsequently used to simulate the micro-crack population and damage evolution in concrete accounting for pore size distribution [20,22,23]. The microstructure of concrete was represented by truncated octahedral cells, which were regarded as the best choice for a regular representation of a solid. The interactions between unit cells were modelled by structural beam elements. One problem of this model is that the relationship between the global elasticity and local element properties cannot be established analytically. To deal with this issue, the site-bond model for elasticity was reformulated by Zhang et al. [24] by using elastic springs instead of beams to represent the microscopic interactions between sites. The relationship between spring constants and macroscopic elastic parameters was analytically derived and validated.

The main purpose of this work is to develop the site-bond technology to study the macroscopic behaviour and damage evolution of cement paste considering its underlying microstructure attributes such as porosity, pore size distribution, volume fraction and particle size distribution of unhydrated cement. X-ray micro-CT along with image processing and analysis techniques is used to capture the microstructure features of cement paste. A site-bond assembly with sites at centres of truncated octahedral cells and bonds connecting the neighbouring cells is applied to represent the microstructure of cement paste, where unhydrated cement particles are placed on each site and pores of different sizes are assigned to bonds according to the measured microstructure features. The simulated microstructure of cement paste is then subjected to different loading conditions. The fracture process and damage evolution are simulated by removing failed bonds. A series of statistical analyses is performed to quantitatively investigate the effects of pore spatial distribution, porosity and pore size distribution on macroscopic mechanical properties and damage evolution. The simulation results are compared with the available experimental data.

2. 3D microstructure of cement paste

This work is focused on pure Portland cement paste without any interfacial transition zone between aggregate and matrix. The microstructure evolution of cement paste due to cement hydration was investigated by using a non-destructive technique, X-ray micro-computed tomography, which is different from other traditional experimental approaches, e.g. optical microscope and scanning electron microscope where sample preparations, such as polishing and drying, may damage the microstructure. Based on a series of image processing and analyses, pore size distribution and particle size distribution of anhydrous cement grains were measured. Details of the extraction techniques are given in the following three sub-sections.

2.1. X-ray micro-computed tomography data

The specimen used here was prepared using ASTM type I Portland cement. The w/c ratio of cement paste specimen is 0.5. After drill mixing in a plastic beaker, small parts of the paste were poured into the syringe and then injected into a micro circular plastic tube with an internal diameter of 250 μm. The micro plastic tube filled with cement paste was sealed and cured under standard conditions until testing. The specimen was scanned at curing ages of 7 and 28 days using a high resolution Xradia MicroXCT-200 CT machine at the Beckman Institute for Advanced Science and Technology at University of Illinois at Urbana-Champaign (UIUC, USA), operating at 50 keV/10 W. The X-ray shadow projections of specimen were digitized as 2000×2000 pixels with a resolution of 0.5 μm and were processed to obtain reconstructed cross-section images using the algebraic method implemented in the Xradia reconstruction software. This resulted in a 3D stack of virtual sections, each consisting of 512×512 voxels with a linear X-ray attenuation coefficient, displayed as an 8-bit image with grey scale values from 0 (black) to 255 (white).

Fig. 1 shows the micro-CT image of a cylinder region with 200 μm in diameter and 100 μm in thickness extracted from the reconstructed 3D image of the 28 days old cement paste. From Fig. 1 some characteristics of cement paste components can be seen. The darkest phases correspond to pores. The brightest phases are anhydrous cement grains. Hydration products are shown as grey.

2.2. Image segmentation

X-ray micro-CT images are composed of voxels, each of which has a unique grey scale value. Prior to morphometrical analysis of the micro-CT images, image segmentation was carried out to identify different phases in hardened cement paste, i.e. pore, hydration product and anhydrous cement grain. A large number of segmentation techniques are available in literature. The most used one is to define a global threshold value based on the grey-level histogram [7]. Voxels that have grey scale values lower or higher than the defined threshold value are considered as

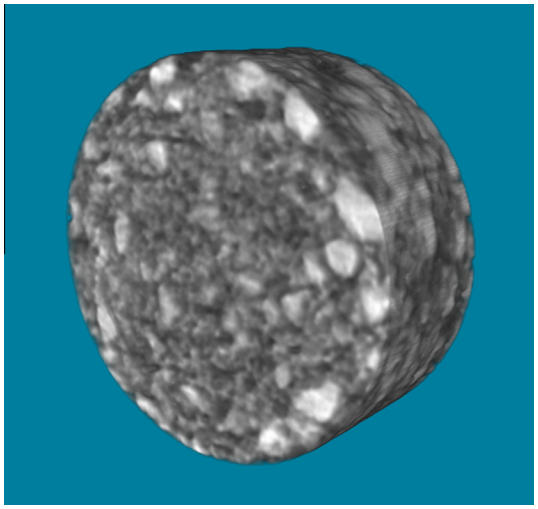

Fig. 1. Micro-CT image of the 28 days old cement paste.

background or object, respectively. In this study, this thresholding method is selected for segmentation purposes. A detailed description of this thresholding method for cement paste can be found in [7].

Fig. 2a illustrates a typical micro-CT slice of cement paste. To avoid the possible edge effects, a cylindrical region of interest (ROI) with a diameter of 476 voxels and thickness of 200 voxels is extracted from the centre of the slices where the cement paste is considered to be the most homogeneous. The grey scale value at the inflection point in the cumulative volume fraction curve of ROI is firstly defined as the threshold value (T_1) to segment pores from solid phases, i.e. hydration products and anhydrous cement grains. This gives rise to a binary image, where pores are shown as black and solid phases are shown as white, as seen in Fig. 2b. Subsequently, a threshold value (T_2) corresponding to the transition points between the two peaks, which are associated with hydration products and anhydrous cement, is determined to separate anhydrous cement grains from other phases. As a consequence, another binary image is obtained, as shown in Fig. 2c. Voxels with grey scale values lower than T_1 is treated as pores. Voxels that have grey scale values higher than T_2 are considered to be anhydrous cement grains. The remaining voxels represents hydration products. Thus, the microstructure of cement paste consisting of pores, hydration products and anhydrous cement grains can be obtained. To illustrate the acquired microstructure, a cubic volume of interest (VOI) of $100 \times 100 \times 100\ \mu m^3$ is taken from the centre of ROI. The 3D microstructure of VOI resulting from image segmentation is shown in Fig. 2d. It can be seen that the original grey scale image is converted into a ternary image of blue, grey and dark red phases which devotes pores, hydration products and anhydrous cement grains, respectively.

2.3. Microstructure features

After image segmentation, the 3D microstructure of cement paste can be quantitatively characterised. In this study, attention is focused on several microstructure features such as porosity, pore size distribution, volume fraction and size distribution of anhydrous cement grains. To obtain these parameters, a series of image analyses is performed using the "Analyze particles" function of ImageJ, a public domain Java-based image processing program (National Institutes of Health, USA).

The binary image derived from image segmentation is replaced by a new 8-bit image including simple outlines of the measured particles by capturing the outlines of phases of interest, e.g., pores and anhydrous cement grains. Fig. 3a and b shows the obtained images containing outlines of pores and anhydrous cement grains corresponding to binary images presented in Fig. 2b and c, respectively.

From this analysis, porosity and volume fraction of anhydrous cement grains are calculated as the ratios of the area inside the outlines to the total area of ROI using area measurements from the binary images. The results of porosity and volume fraction of anhydrous cement grains for cement paste specimens with curing ages of 7 and 28 days are listed in Table 1. Both porosity and volume fraction of unhydrated cement decrease gradually with increasing curing age due to the progress of cement hydration.

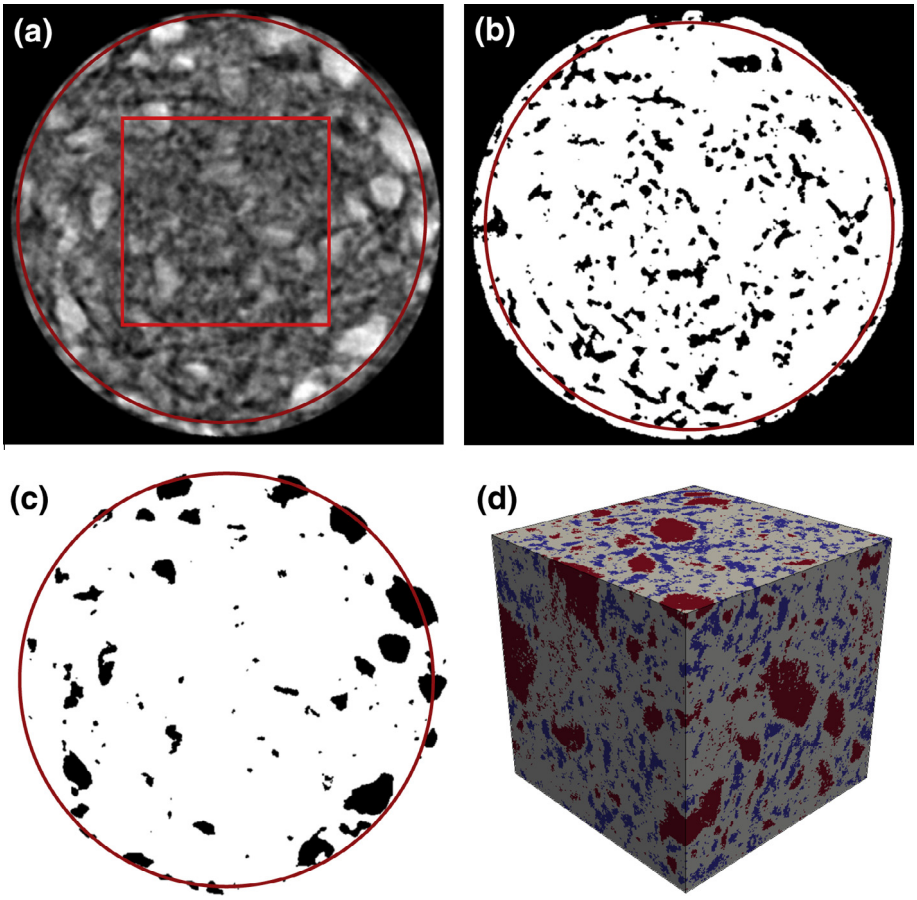

Fig. 2. Illustration of image segmentation: (a) micro-CT image; (b) pore phase; (c) anhydrous cement grain; (d) 3D microstructure of volume of interest ($100 \times 100 \times 100\ \mu m^3$).

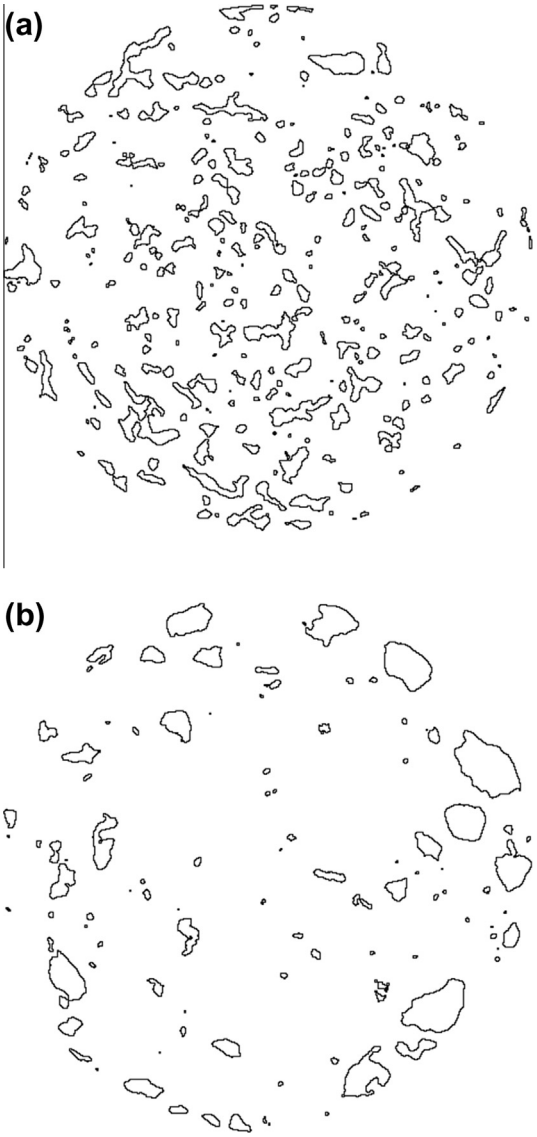

Fig. 3. Outlines of the measured phases: (a) pore; (b) anhydrous cement grain.

Table 1
Porosity and volume fraction of anhydrous cement grains of cement pastes at various curing ages.

	Curing ages	
	7 days	28 days
Porosity (%)	18.72	12.58
Volume fraction of anhydrous cement grains (%)	15.67	8.65

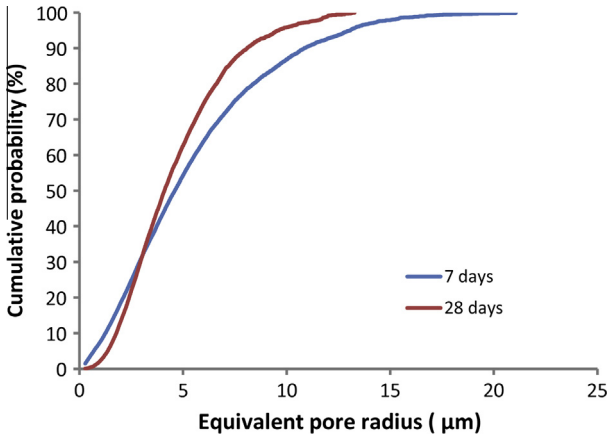

Fig. 4. Pore size distribution of cement pastes with various curing ages.

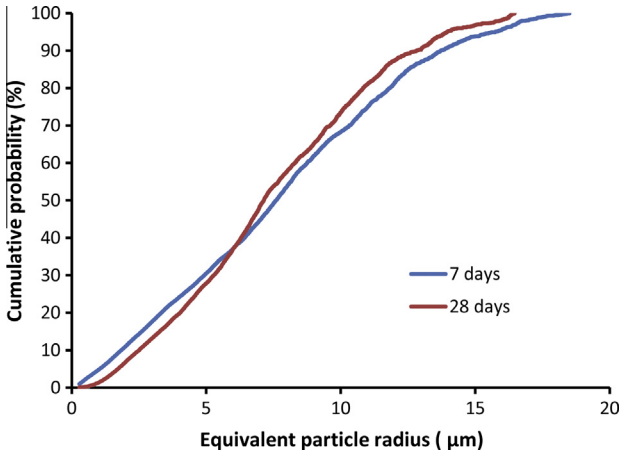

Fig. 5. Particle size distribution of unhydrated cement of cement pastes with various curing ages.

The construction of the microstructure-informed site-bond model, Section 3, is based on a random allocation of features, unhydrated cement particles and pores, with sizes belonging to the experimentally measured distributions. Assuming spherical shapes for pores and particles, the experimental sizes (radii) were calculated from the measured areas of the corresponding segmented features, example in Fig. 3. The sizes of the features, c_i, were used to construct cumulative probability distributions with standard median ranking, where for n features with sizes ordered as $c_1 \leqslant c_2 \leqslant \ldots \leqslant c_n$, the cumulative probability for features with sizes less than c_i is given by $F(c < c_i) = (i - 0.3)/(n + 0.4)$. Figs. 4 and 5 show the obtained cumulative probability functions for pore and unhydrated cement particle sizes of cement paste specimens at ages of 7 and 28 days. It can be seen that both the sizes of largest pore and particle, and fractions of large pores and unhydrated cement particles all decrease with the increase of curing age. For the random allocation of pore and particle sizes to the model, a generator of uniformly distributed random numbers $0 \leqslant p < 1$ is used. For a given p, the calculated size of a feature is $c = F^{-1}(p)$, which is performed by interpolation between experimental data points. The process ensures that the distribution of features sizes in the model comes from the same population as in the experiment.

3. Site-bond model

3.1. Discrete representation of material volume

In the site-bond model [20–24], a material volume is represented by an assembly of truncated octahedral cells, each of which has six square and eight regular hexagonal faces, as illustrated in Fig. 6a. The centre of each unit cell is regarded as a site, which is connected to its neighbouring sites by fourteen bonds. These bonds are classified into two groups: B_1 consists of six bonds in principal directions (normal to the square faces) and B_2 comprises eight bonds in octahedral directions (normal to the hexagonal faces), as illustrated in Fig. 6b. In this work, the bonds are modelled with elastic-brittle normal and shear springs to represent the relative

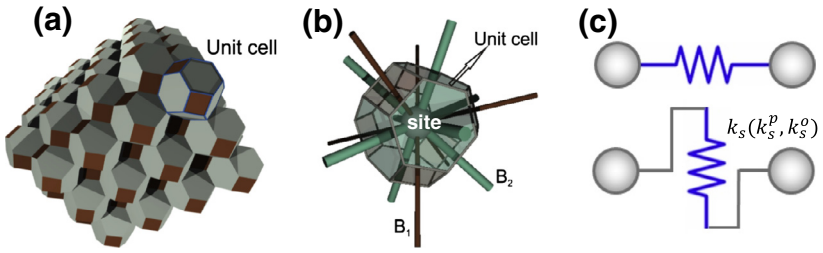

Fig. 6. Cellular lattice: (a) site-bond assembly; (b) unit cell with bonds; (c) normal and shear springs.

deformations between two adjacent cells, as presented in Fig. 6c. This is sufficient for the loading cases used; the addition of angular-type springs resisting twist and bending deformations is under development for applications to more general loading cases.

3.2. Spring elastic properties

The starting point for the derivation of the elastic spring constants is the equivalence of the strain energy stored in a unit cell of volume V between the discrete (U_{disc}) and the continuum system (U_{cont}),

$$U_{disc} = U_{cont} \tag{1}$$

We use a linear homogeneous displacement field for deriving the spring constants, i.e. the components of the displacement vector are arbitrary linear functions of the coordinates. Non-linear displacement fields, introducing rotations and curvatures, would activate the potential angular springs, which is outside the scope of the present study. Under the assumed displacement field, the strain energy in the continuum cell is given by.

$$U_{cont} = \frac{1}{2}\int_V \sigma\varepsilon dV = \frac{1}{2}C_{ijkl}\varepsilon_{ij}\varepsilon_{kl}V \tag{2}$$

where C represents the stiffness tensor of the material, ε is the strain field. The strain energy stored in the discrete cell is

$$\begin{aligned} U_{disc} &= \frac{1}{4}\sum_{b=1}^{14}\left(k_n^{(b)}u_n^{(b)}u_n^{(b)} + k_s^{(b)}u_s^{(b)}u_s^{(b)}\right) \\ &= \frac{1}{4}\sum_{b=1}^{14}(L^{(b)})^2\left(k_n^{(b)}\xi_i^{(b)}\varepsilon_{ij}\xi_j^{(b)}\xi_k^{(b)}\varepsilon_{kl}\xi_l^{(b)}\right. \\ &\quad \left. + k_s^{(b)}\left(\varepsilon_{kl}\xi_l^{(b)} - \xi_i^{(b)}\varepsilon_{ij}\xi_j^{(b)}\xi_k^{(b)}\right)\left(\varepsilon_{km}\xi_m^{(b)} - \xi_n^{(b)}\varepsilon_{nm}\xi_m^{(b)}\xi_k^{(b)}\right)\right) \end{aligned} \tag{3}$$

where the superscript b represents the b_{th} bond (spring), N_b is the total number of bonds, $k_n^{(b)}$ and $k_s^{(b)}$ denotes the constants of normal and shear springs, $u_n^{(b)}$ and $u_s^{(b)}$ stand for the corresponding relative displacements, $L^{(b)}$ is the length of bond b, $\xi_i^{(b)}$ is the direction vector. Note that the factor is 1/4, because only half of the spring lengths belong to the unit cell.

From Eqs. (1)–(3), the following relation is easily derived

$$C_{ijkl} = \frac{1}{2V}\sum_b^{N_b}\left(L^{(b)}\right)^2\left(k_s^{(b)}\delta_{ik}\xi_j^{(b)}\xi_l^{(b)} + \left(k_n^{(b)} - k_s^{(b)}\right)\xi_i^{(b)}\xi_j^{(b)}\xi_k^{(b)}\xi_l^{(b)}\right) \tag{4}$$

where δ_{ik} is the Kronecker's delta.

For the site-bond assembly shown in Fig. 6, if the spacing between two adjacent sites in principal directions is denoted by L, bonds B_1 and B_2 have lengths of L and $\sqrt{3}L/2$, respectively. The volume of the unit cell V equals $L^3/2$. The model length scale, L, is dictated by microstructure characteristics as described in Section 4. Each bond has one normal spring and two shear springs. The two shear springs of one bond have the same stiffness coefficient. The spring constants are denoted by k_n^p and k_s^p, k_n^o and k_s^o for principal bonds B_1 and octahedral bonds B_2, respectively. The unit cell bond vectors $\xi_i^{(b)}$ are given in Table 2.

Table 2
Direction vectors of bonds of the site-bond assembly.

Bond B_1		Bond B_2	
b	$\xi_i^{(b)}$	b	$\xi_i^{(b)}$
1	(1, 0, 0)	1	$(1/\sqrt{3}, -1/\sqrt{3}, -1/\sqrt{3})$
2	(0, 1, 0)	2	$(1/\sqrt{3}, 1/\sqrt{3}, -1/\sqrt{3})$
3	(0, 0, 1)	3	$(1/\sqrt{3}, -1/\sqrt{3}, 1/\sqrt{3})$
4	(−1, 0, 0)	4	$(1/\sqrt{3}, 1/\sqrt{3}, 1/\sqrt{3})$
5	(0, −1, 0)	5	$(-1/\sqrt{3}, 1/\sqrt{3}, 1/\sqrt{3})$
6	(0, 0, −1)	6	$(-1/\sqrt{3}, -1/\sqrt{3}, 1/\sqrt{3})$
		7	$(-1/\sqrt{3}, 1/\sqrt{3}, -1/\sqrt{3})$
		8	$(-1/\sqrt{3}, -1/\sqrt{3}, -1/\sqrt{3})$

Substitution of these into Eq. (4) provides the following relation between the stiffness tensor components and the spring constants

$$C_{1111} = \frac{2}{3L}\left(3k_n^p + k_n^o + 2k_s^o\right) = C_{2222} = C_{3333} \tag{5}$$

$$C_{1122} = \frac{2}{3L}\left(k_n^o - k_s^o\right) = C_{1133} = C_{2233} = C_{2211} = C_{3311} = C_{3322} \tag{6}$$

$$C_{1212} = \frac{2}{3L}\left(3k_s^p + k_n^o + 2k_s^o\right) = C_{1313} = C_{2323} = C_{2121} = C_{3131} = C_{3232} \tag{7}$$

$$\text{Other } C_{ijkl} = 0 \tag{8}$$

With the Voigt notation, the spring constants are can be expressed as

$$k_n^p = -k_n^o + \frac{L}{2}(C_{11} + 2C_{12}) \tag{9}$$

$$k_s^p = -k_n^o + \frac{L}{2}(2C_{12} + C_{44}) \tag{10}$$

$$k_s^o = k_n^o - \frac{3L}{2}C_{12} \tag{11}$$

Thus, the four normal and shear stiffness coefficients of the bonds are related to three constants, representing cubic elasticity. For cubic elasticity, the stiffness tensors can be given in terms of the bulk modulus K and two shear moduli G_1 and G_2 as follows

$$C_{11} = K + \frac{4}{3}G_2 \tag{12}$$

$$C_{12} = K - \frac{2}{3}G_2 \tag{13}$$

$$C_{44} = G_1 \tag{14}$$

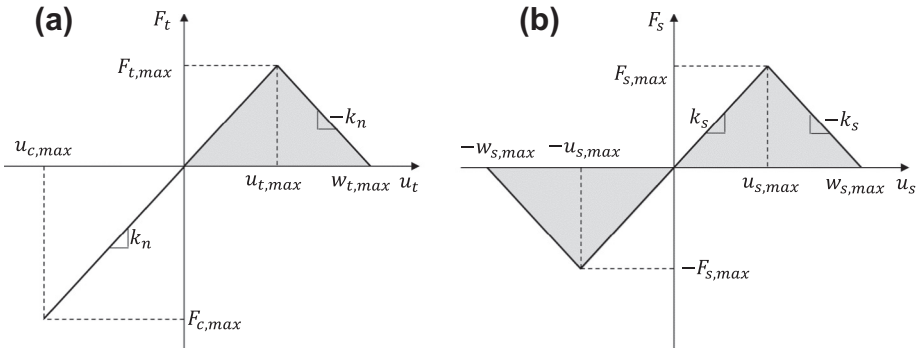

Fig. 7. Constitutive model and failure criteria for springs: (a) normal springs; (b) shear springs.

Hence in the most general case the proposed spring-based site-bond model could represent materials with cubic elasticity with prescribed bulk and shear moduli. The system for determining spring constants, however, is over-determined. Out of the infinitely many possibilities to resolve the over-determinacy, we select the stiffness coefficient for shear springs of bonds B_1, k_s^p, to be zero, since the contribution of k_s^p to macroscopic elasticity can be represented in terms of k_s^o, as seen in Eqs. (9)–(11). From this all materials with cubic elasticity that can be represented by the model can be derived. Our interest is in isotropic materials, for which the bulk and shear moduli are related to Young's modulus E and Poisson's ratio v as: $K = E/(3(1-2v))$ and $G_1 = G_2 = G = E/(2(1+v))$. Thus the spring constants are determined as follows

$$k_s^p = 0; \quad k_n^p = \frac{EL}{4(1+v)(1-2v)};$$
$$k_n^o = \frac{(1+2v)EL}{4(1+v)(1-2v)}; \quad k_s^o = \frac{(1-4v)EL}{4(1+v)(1-2v)} \tag{15}$$

The result shows that the proposed lattice can represent any isotropic elastic material with Poisson's ratio in the range $-1/2 \leqslant v \leqslant 1/4$, if all spring stiffness coefficients are required to be non-negative. This is significant improvement over previous regular lattices, where only isotropic materials with zero Poisson's ratio could be represented in [8,19]. For materials with Poisson's ratio higher than 1/4, the negative shear spring constant required seem to be non-physical. However, it was found that the negative stiffness coefficient has a physical explanation at the molecular level [25]. Therefore, a negative k_s^o in this scheme can be used to model a material with a Poisson's ratio higher than 1/4 but lower than 1/2, which covers most of engineering materials.

To validate the derived spring constants, two benchmark tests including uniaxial tension and plane-strain tension were performed in a previous work [24]. It was shown that the simulated macroscopic Young's modulus, Poisson's ratio and shear modulus converged to the theoretical values, i.e. the boundary effects became negligible, when the size of cubic site-bond assembly was larger than $15L \times 15L \times 15L$. Hence, a model of cubic region with size of $20L \times 20L \times 20L$ will be used in the following simulations.

3.3. Spring elastic-brittle behaviour

The spring elastic-brittle behaviour is represented by linear elastic and linear softening branches separated by a damage initiation point. The elasticity is dictated by Eq. (16) for given macroscopic elastic properties and microstructure-related length scale. The softening branch approximates the local post-initiation resistance of the matrix to failure. The adopted constitutive models for normal and shear springs are illustrated in Fig. 7, where $u_{t,max}$ and $u_{s,max}$ represent the deformation of the normal and shear springs at damage initiation with corresponding maximum normal $F_{t,max}$ and shear forces $F_{s,max}$; $W_{t,max}$ and $W_{s,max}$ represent the deformation of the normal and shear springs at failure (set to $2u_{t,max}$ and $2u_{s,max}$, respectively); $k_n = F_{t,max}/u_{t,max}$ is the stiffness coefficient of the normal spring and $k_s = F_{t,max}/u_{t,max}$ is the stiffness coefficient of the shear spring. For normal springs, failure in compression is not allowed, which is achieved by setting the critical compressive deformation as $u_{c,max} = -10u_{t,max}$ and the maximum compressive force as $F_{c,max} = -10F_{t,max}$. With these settings, the spring behaviour is fully controlled by prescribed local failure energy, G_f shaded in grey in Fig. 7.

The effect of cement porosity is introduced via the failure energies of the springs. The bonds are assigned notional areas equal to the areas of their corresponding faces in the cellular structure. For each bond of the model, the failure energy is calculated by $G_f = 2\gamma A_e$, where γ denotes the surface energy of the material and A_e is the effective area of the face, i.e. the difference between the original face area (A_0) and the cross-section area of pores assigned to the face (A_p) as described in Section 4. The failure energy assigned to the normal and shear springs in a bond is presently the same.

4. Modelling and simulation

In this study, a material volume of size $20L \times 20L \times 20L$ is used. The corresponding cellular structure contains 17,261 cells; the site-bond model has the same number of sites and 113,260 bonds. The microstructure of cement paste is modelled as a three-phase composite structure consisting of anhydrous cement grains, hydration products and pores. Anhydrous cement grains are located at the centres of all cells. Other places in cells are occupied by hydration products, in which pores with sizes ranging from zero to the maximum pore size are involved and reside notionally at the interfaces between cells. The anhydrous cement grains and the hydration products provide a combined elastic response. The properties of hydration product are averaged over all types of hydrates, including calcium silicate hydrates (C–S–H), portlandite (CH) and ettringite (AFt) of different mass densities. The macroscopic elastic parameters, Young's modulus E and Poisson's ratio v, and the surface energy γ are taken from literature. These are generally obtained from nano-indentation tests and X-ray photoelectron spectroscopy measurements, respectively. The values used in our simulations are given in Table 3 with the corresponding references.

4.1. Microstructure incorporation

The microstructure information obtained experimentally is introduced into the site-bond model in two steps:

Table 3
Macroscopic elastic constants and surface energy of different phases.

Phase	E (GPa)	ν	γ (mJ/m^2)	Source
Hydration product	29.2	0.24	50	[26,27]
Anhydrous cement grain	139.9	0.30	–	[18]
Pore	0	0	–	–

Step I: The volume fraction and particle size distribution of anhydrous cement grains measured from X-ray micro-CT scans (Fig. 5 and Table 1) are used for calculating the model length scale, L. Anhydrous cement grains of different sizes are assigned randomly to all sites of the cellular structure according to the experimental particle size distribution. A generator of uniformly distributed random numbers $0 \leqslant r < 1$ is used to assign grains with different sizes to individual sites. For each site, a random number r is generated and the assigned grain size is derived as $R_i = F^{-1}(r)$, where $F(R_i)$ is the cumulative probability of grain sizes presented in Fig. 5. A comparison of simulated and experimental particle size distributions is shown in Fig. 8. This process ensures that the simulated grain size distribution of anhydrous cement fits the measured size distribution from X-ray micro-CT scans very well. In terms of shape, anhydrous cement grains are assumed to be spherical. As a result, each cell has one spherical anhydrous cement grain with size of R_i.

The cell size is calculated from the volume fraction of anhydrous cement grains, ϕ_a, and the volume of the cellular structure with N cells via $\phi_a NL^3/2 = \sum_i 4\pi R_i^3/3$. The stiffness coefficients of normal and shear springs in each bond are calculated from the given macroscopic Young's modulus E, Poisson's ratio ν and the determined cell size L using Eq. (15).

Step II: The porosity and pore size distribution measured from X-ray micro-CT scans (Fig. 4 and Table 1) are used for calculating the bond failure energies. Pores are assigned randomly to the bonds using the same method described in Step I. Notionally, the assignment is to the faces of the cellular structure, but the process does not constrain the pore positions; these could be anywhere in the region belonging to a bond. The assignment continues until the prescribed porosity in the modelled material volume is reached. The critical failure energy of bonds is calculated from the prescribed surface energy and the intact area associated with the bond via $G_f = 2\gamma A_e$, as explained in Section 3.3. Thus, all bonds of given type have the same elastic spring constants but different critical failure energy due to the different pore sizes assigned. Due to the existence of pores with different sizes in bonds, the critical failure energy of each bond varies from the maximum failure energy $2\gamma A_0$ for pore size of zero to zero for pore area close to the intact area of the face, e.g. square face or hexagonal face. If the pore area in a bond is equal to or larger than the corresponding face area, this bond is removed before loading.

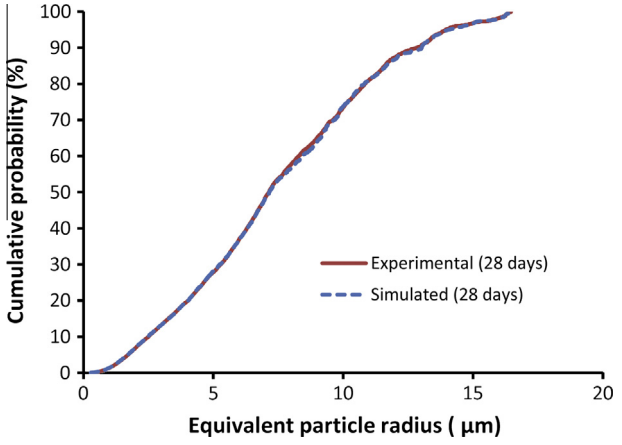

Fig. 8. Comparison between the simulated and experimental particle size distributions of 28 days old cement paste.

4.2. Boundary conditions

Two loading cases, uniaxial tension and plane strain, are considered in this work. The former is used to compare predictions for stress–strain behaviour to available experimental data. The latter is used to demonstrate expected behaviour of the material ahead of a macroscopic crack, where plain strain conditions prevail. The loads are applied via prescribed displacements to the boundary sites of the site-bond model. Considering a coordinate system (X_1, X_2, X_3), the displacements and reaction forces of sites on the boundaries are referred to as (u_1, u_2, u_3) and (F_1, F_2, F_3), respectively. For uniaxial tension, the sites on $X_1 = 0$, $X_2 = 0$ and $X_3 = 0$ are fixed in the X_1-, X_2- and X_3-directions, respectively. A displacement of $u_1 = L$ which corresponds to a strain of $\varepsilon = L/20L = 0.05$ is imposed at $X_1 = 20L$. Other sites are free. For plane strain, the sites on $X_1 = 0$, $X_2 = 0$, $X_3 = 0$ and $X_3 = 20L$ are fixed in the X_1-, X_2- and X_3-directions, respectively. Constant displacements of $u_1 = L$ and $u_2 = L$ are applied at $X_1 = 20L$ and $X_2 = 20L$, respectively.

4.3. Numerical simulations and macroscopic damage measures

The simulations of damage evolution are performed by using an in-house code in association with Abaqus. The in-house code is used to control the failure of bonds. Abaqus is used as a solver to get repetitive solutions for equilibrium. At each load step, the in-house code obtains the forces, deformations and calculates bond energies. The bond fails when its energy reaches the assigned failure energy, mimicking the creation of a micro-crack along the interface between the two cells joined by the bond. Upon failure the bond is removed from the site-bond assembly. After this update the assembly is solved by Abaqus for equilibrium. This results in a redistribution of forces in the structure and consecutive failures of bonds. The simulation is continued until all bonds fail or the prescribed strain is met. The macroscopic damage is thus emerging from the generation and evolution of micro-crack population.

The macroscopic stresses at each load step are calculated by dividing the corresponding total reaction forces by the boundary area. To quantitatively describe the damage evolution, some scalar damage parameters are required. The standard damage variable, D_E is defined as the relative change in Young's modulus as follows

$$D_E = 1 - \frac{E_i}{E_0} \tag{16}$$

where E_0 denotes the initial (undamaged) elastic modulus, and E_i stands for the current (damaged) modulus. In the beginning, D_E is equal to zero when the bonds are intact and finally turn into one when all of the bonds fail. To capture possible development of damage-induced anisotropy, four additional damage variables are introduced measuring relative changes in bulk and shear moduli

$$D_K = 1 - \frac{K_i}{K_0} = \frac{(\sigma_h/\varepsilon_v)_i}{(\sigma_h/\varepsilon_v)_0} \tag{17}$$

$$D_G = 1 - \frac{G_i}{G_0} = \frac{(s_j/e_j)_i}{(s_j/e_j)_0} \qquad s_j = \sigma_j - \sigma_h; \quad e_j = \varepsilon_j - \varepsilon_v \quad (j = 1,2,3) \tag{18}$$

where σ_h and ε_v represent the hydrostatic stress and volumetric strain, respectively, S_j and e_j are the deviatoric stress and strain, respectively.

5. Results and discussion

5.1. Damage evolution under uniaxial tension

Fig. 9 shows the simulated stress–strain curve of a generated cement paste specimen at 28 days of curing under uniaxial tension using the aforementioned modelling procedure. On a single 64-bit PC (Processor: 2.0 GHz, RAM memory: 32 GB), the simulation time for this case is about 3 h. As seen in Fig. 9, the initial elastic part is perfectly linear followed by a "graceful" non-linear response prior to the peak point. From this curve, some important parameters such as global elastic modulus, tensile strength, strain at peak point and fracture energy of cement paste can be obtained, which can be used as input to estimate the mechanical properties and fracture process of cementitious materials at a coarser length scale, e.g. mortar and concrete. The elastic modulus is the slope of the stress–strain curve at the linear elastic stage. The tensile strength and peak strain correspond to tensile stress and strain at peak point, respectively. The fracture energy can be determined by integrating the area below the stress–strain curve. The fracture energy is a primary parameter for continuum-based fracture models, e.g. cohesive zone model. In this work, attention is placed on the tensile strength and damage evolution.

Fig. 10 shows the development of the damage variables, i.e. D_E, D_K and D_G, defined in Section 4.3 with the applied strain. It can be seen that the damage parameter D_E based on the relative reduction of the Young's modulus is equal to the damage parameters D_K and D_G based on the relative changes of the hydrostatic stress and the three components of the deviatoric stress. This indicates that the simulated cement paste specimen maintains macroscopic isotropy during damage evolution under uniaxial tensile loading. When the deformation is small, the damage variables remain close to zero with few isolated local failures. With the increase of deformation, the growing population of micro-cracks drives the increase of the macroscopic damage. The initially slow damage growth is still associated with isolated local failures. This regime is followed by a more rapid increase of damage after approximately 1×10^{-4} applied strain, associated with micro-crack coalescences. The failure of the specimen occurs at approximately 8% damage, which is a result of an "avalanche"-like, i.e. nearly instantaneous, failure of a set of bonds critical for the specimen integrity.

Comparison between Figs. 9 and 10 suggests that the isolated failures have negligible effect on the non-linear stress–strain response and observable non-linearity occurs with micro-crack growth via coalescence. The avalanche-failure characterises the peak in the stress–strain response. It should be noted that the post-peak softening response, sometimes demonstrated by authors with different modelling approaches, was not achieved under tensile loading with the proposed simulation methodology as it would require computationally expensive short increments to separate failing bonds close to specimen failure. This was outside the purpose of the work.

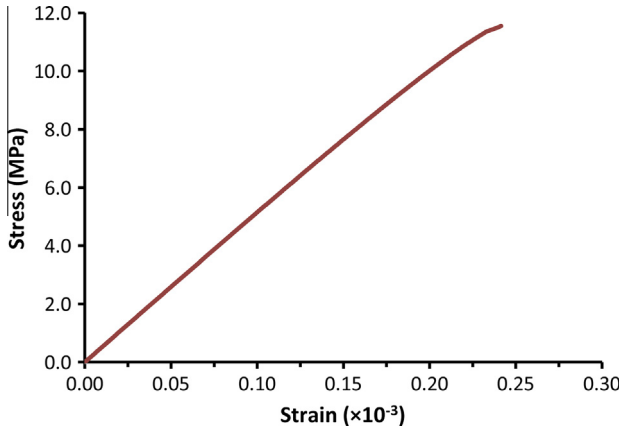

Fig. 9. Simulated stress–strain curve of 28 days old cement paste under uniaxial tension.

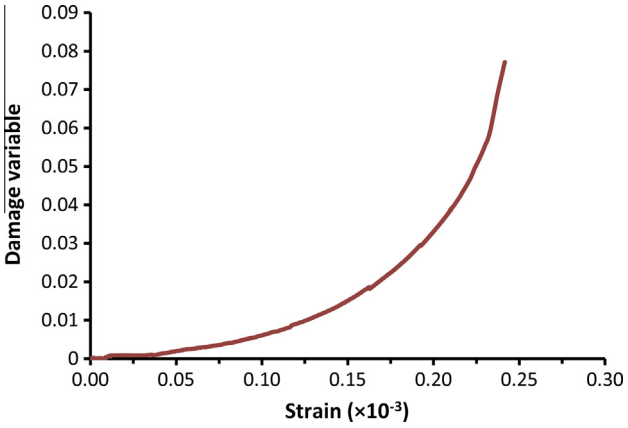

Fig. 10. Damage evolution in 28 days old cement paste under uniaxial tension.

5.2. Damage evolution under plane strain

Fig. 11 shows the predicted stress–strain response of cement paste at 28 days of curing under plane strain. Non-linearity is hardly observed and the specimen fails in an almost perfectly brittle manner. The difference from uniaxial tension can be explained with the fact that in the case of plane strain each bond in the site-bond assembly is subjected to a higher combined action of transverse tension stress and shear stress at a same load step compared to that under uniaxial tension, and the bonds are broken more rapidly and suddenly. As a result, both the tensile strength and strain at peak point of the specimen are lower, as shown in Fig. 11.

The corresponding evolution of damage parameters is illustrated in Fig. 12. The damage parameters D_{G1}, D_{G2} and D_{G3} denote the relative changes of the longitudinal shear moduli in X_1-, X_2- and X_3- directions, respectively. It can be seen that the values of the damage parameters are low at the failure point, which determines the glass-like mechanical response. This results from an early avalanche-like failure of bonds and implies more brittle characteristic of cement paste under plane strain. In addition, the

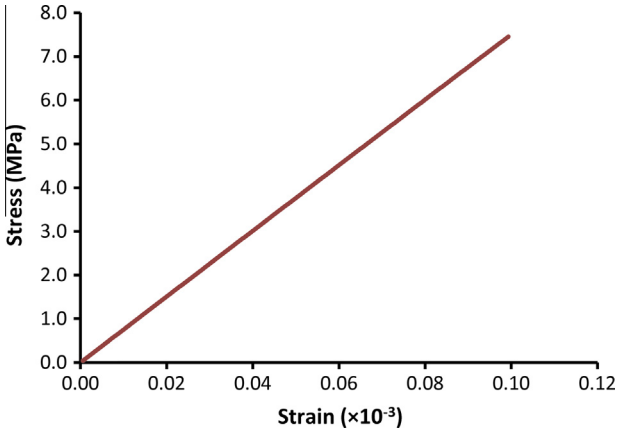

Fig. 11. Simulated stress–strain curve of 28 days old cement paste under plane strain.

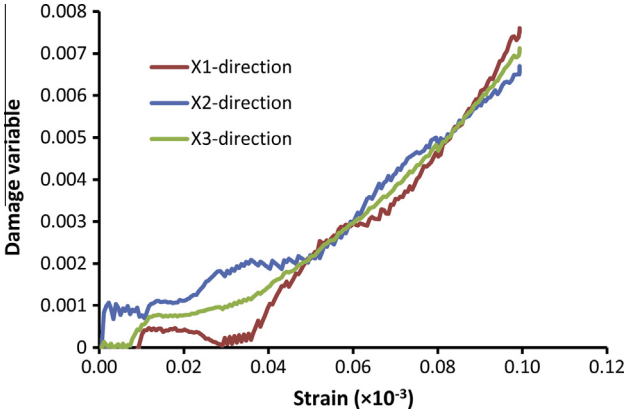

Fig. 12. Damage evolution in 28 days old cement paste under plane strain.

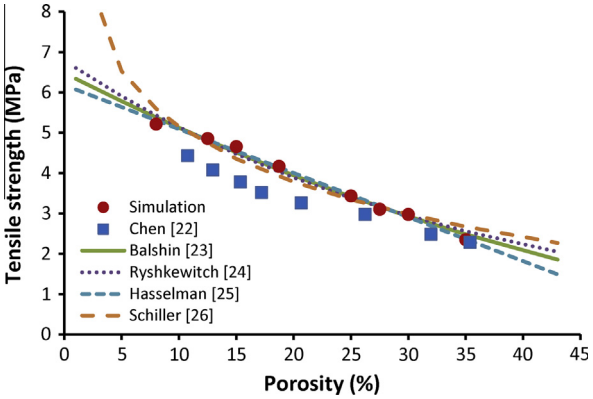

Fig. 13. Relationship between tensile strength and porosity of cement paste.

development of damage in different directions is different, which illustrates that under plane strain the generated micro-crack population yields damage-induced anisotropy in the cement paste specimen. The directional dependence of damage evolution in the specimen can be explained by the fact that the generated microstructure of cement paste specimen is heterogeneous due to the different assigned pore sizes on different bonds. Further insight into this aspect is obtained by statistical analyses as presented in the following sections.

5.3. Influence of pore spatial distribution

Pores are considered as initial defects before mechanical loading. To investigate the influence of random distribution of pores in location on mechanical properties and damage evolution, a set of 40 cement paste samples with curing age of 28 days are generated. The measured porosity and volume fraction of anhydrous cement grains are 12.58% and 8.65%, respectively. The pore size distribution and particle size distribution of unhydrated cement are shown in Figs. 4 and 5. These parameters are fixed for sample generation. Because the spatial distribution of pores in the system is random, the corresponding simulated microstructures of cement paste represented by the site-bond assembly are different. These samples are then subjected to uniaxial tensile loading and the tensile strength is obtained.

Here, the statistical parameters such as mean value, standard deviation and coefficient of variation of tensile strength for all the 40 cement paste samples are calculated from the simulated results. An average tensile strength of 6.96 MPa is found for 28 days old cement paste with w/c of 0.5 (porosity is 12.58%). This is consistent with the experimental results reported by Robler and Odler [28], who measured the tensile strength of cement paste specimens at different curing ages with various w/c ratios. It was presented that the tensile strength of 28 days old specimens with w/c ratios of 0.47 and 0.52 is 9 MPa and 6 MPa, respectively, the corresponding porosities of which are 11.1% and 13.3% [28]. The coefficient of variation in tensile strength is approximately 5%, which indicates that the random spatial distribution of initial defects (pores) in the specimen has a negligible effect on the mechanical properties of cement paste and damage evolution.

5.4. Influence of porosity

To study the influence of initial defects amount on mechanical properties and damage evolution in a quantitative manner, a series of 7 days old cement paste samples with identical volume density and particle size distribution of unhydrated cement, and pore size distribution (see Table 1 and Figs. 4 and 5) but different porosities ranging from 8% to 35% are generated. For each porosity, a set of 40 cement paste samples are simulated. Fig. 13 shows the average tensile strength as a function of the porosity of cement paste. As expected the tensile strength decreases with the increase of porosity.

For the purpose of comparison, the experimental data of tensile strength against the porosity of cement paste taken from Chen et al. [29] are also plotted in Fig. 13. The correlation coefficient between the simulation results and experimental data equals to 0.98 which implies that the simulation results show a very good agreement with the experimental data, especially for the specimens with porosity higher than 20%.

In the past decades, several equations have been proposed to estimate the relationship between tensile strength and porosity of cement-based materials. The four most commonly used equations are listed as follows with the corresponding Refs. [30–33]

$$\begin{aligned} f_t &= f_0(1-\phi_p)^a && \text{Balshin [30]} \\ f_t &= f_0 e^{-a\phi_p} && \text{Ryshkewitch [31]} \\ f_t &= f_0 - a\phi_p && \text{Hasselman [32]} \\ f_t &= b\ln(\phi_0/\phi_p) && \text{Schiller [33]} \end{aligned} \tag{19}$$

where f_t is the strength at zero porosity, a and b are empirical constants, and f_0 represents the porosity at zero strength.

These four equations are presented in Fig. 13 as well to demonstrate how the proposed model compares to previous studies. It is clear that strength–porosity curves resulted from any of the four equations are very similar in the range of the simulated porosities. An excellent relationship between the simulation results and calculated values was observed for each of the given equations. After fitting the simulation results it is found that the tensile strength–porosity relationship of cement paste can be expressed most accurately using the linear Hasselmann's equation ($f_t = 6.18 - 0.11\phi_p$) with a coefficient of correlation of 0.995.

Fig. 14 illustrates the evolution of the damage parameter D_E with increasing applied strain for cement paste specimens with porosities of 8%, 18.72% and 35%. The value of D_E for all porosities initially remains steady at zero and then gradually increases with the increase of the applied strain. For specimens with higher porosities, the rate of damage evolution is greater and the specimen fails earlier, which can be attributed to the more rapid propagation and coalescence of micro-cracks in cement paste with increasing amount of pores. Moreover, there appears a similar damage evolution rate for specimens with porosities of 18.72% and 35% prior to final failure. When the applied strain reaches about 0.18 ($\times 10^{-3}$), the 35% porosity specimen exhibits a sharp increase in the damage

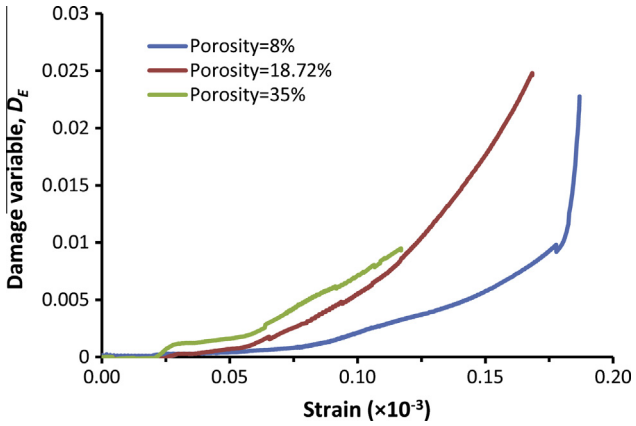

Fig. 14. Damage evolution in cement paste specimens with various porosities.

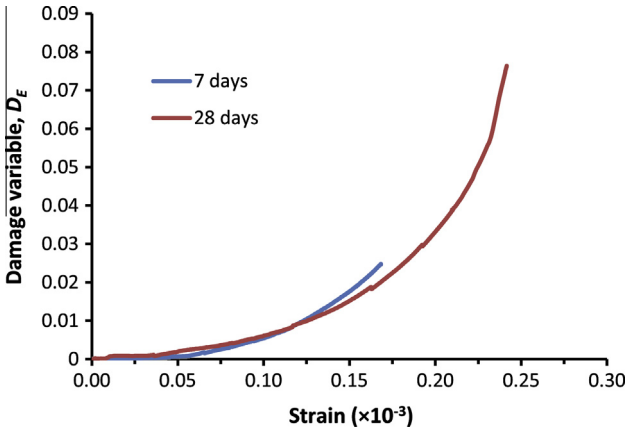

Fig. 16. Damage evolution in cement paste specimens with curing ages of 7 and 28 days.

evolution rate. This corresponds to the sudden simultaneous rupture of bonds in the system.

5.5. Influence of pore size distribution

Besides the random arrangement and amount of pores, other factors affecting potentially the mechanical behaviour the development of damage in cement paste are pore size distribution, volume density and particle size distribution of unhydrated cement. This information can be extracted from cement paste specimens with different curing ages. To estimate the effects of such factors, simulations are carried out on the specimens with curing ages of 7 and 28 days. It is found that the calculated cell size L according to the method presented in Section 4 for these two specimens is very similar, approximately 20 μm, although their volume density and particle size distribution of unhydrated cement particles are different. It should be noted that this outcome is specific to the experimental data used, where the changes in particle size distribution and volume density lead to a combined negligible effect on the model length scale. The outcome could be different for different cement types.

Fig. 15 shows the simulated stress–strain curves for specimens under uniaxial tensile loading. For the 7 days old specimen, very little non-linearity is observed and it tends to fail suddenly and in a strictly brittle manner compared to the 28-day old specimen. The corresponding development of D_E is presented in Fig. 16. The damage evolution in two specimens follows a very similar path. However, the value of D_E prior to failure for 7-day old specimen is much lower than that for 28-day old specimen. This result can be explained by the fact that the 7-day specimen has a higher porosity than the 28-day old specimen and more large pores are assigned to bonds. Hence, more bonds in the system have lower critical failure energies and tend to fail more quickly. As a consequence, the 7-day specimen exhibits a more brittle response than 28-day old specimen under uniaxial tension.

The main difference between the generated site-bond assemblies for these specimens is the random distribution of pores in space, porosity and pore size distribution in the system. The effects of the first two factors have been discussed above. Therefore, this section is focused on the influence of pore size distribution. As presented in Section 5.3, the average tensile strength of 28-day old cement paste is 6.96 MPa, the porosity of which is 12.58%. For comparison, the porosity of 7-day old cement paste is set to 12.58% as well. According to the derived linear relation between tensile strength and porosity, the strength of the 7-day old cement paste should be the same as for the 28-day old cement. However, the simulations provided a tensile stress of the 7-day old cement paste of 6.17 MPa, which is 11.4% lower than the tensile strength of 28-day old cement paste. This difference is entirely attributed to the different pore size distribution in these two specimens. This result suggests that the linear porosity tensile strength relation is valid only for media with identical distribution of pore sizes. More general relation between porosity, pore size distribution and tensile strength (as well as fracture energy) is subject of ongoing work.

Some quantitative assessment of the observed behaviour is offered with Fig. 17, which shows the probability density of pore

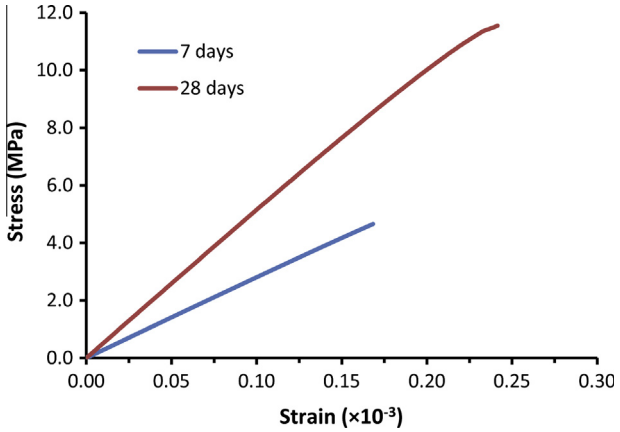

Fig. 15. Simulated stress–strain curve of 7 days and 28 days old cement pastes under uniaxial tension.

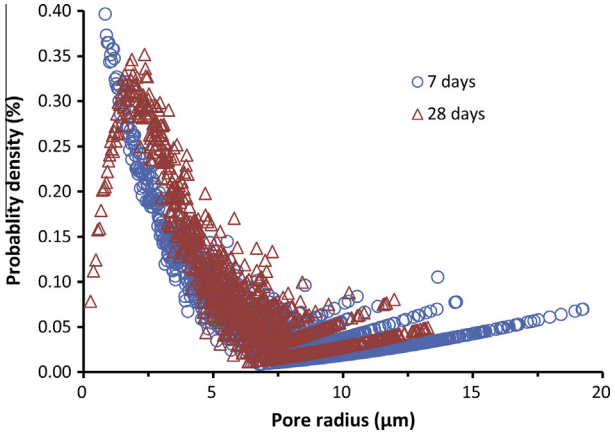

Fig. 17. Probability density of pore sizes in specimens with curing ages of 7 and 28 days.

sizes in specimens with curing ages of 7 and 28 days. It is clear that the volume fraction of large pores in the 7-day old specimen is much higher than that in the 28-day old specimen. Moreover, the largest pore size in the 7-day old specimen is about 20 μm, which is greater than the maximum pore size of 13 μm in the 28-day old specimen. The largest pore size is frequently of interest in investigation of fracture behaviour of cementitious materials. Here, specimens with the same overall porosity but different pore size distribution have different tensile strengths demonstrates that the size and volume fracture of large pores play a critical role in overall rupture strength. This agrees very well with the basic fracture theory suggesting that the largest flaw should determine the fracture strength.

5.6. General discussion

In this work, cement paste was considered as a three-phase composite, consisting of anhydrous cement grains, hydration products and pores. The changes in the microstructure of cement paste were reflected solely by the changes of volume fractions, size and spatial distribution of each phase from tomography data at various curing ages. Although progress is continuously made in X-ray CT technique, it is still a big challenge to identify different hydrates in hydration product, such as high-/low-density calcium silicate hydrates (C–S–H), portlandite (CH) and ettringite (AFt). It is even a bigger challenge to obtain the mechanical properties of different phases required for our modelling approach. Therefore, in this study, the hydration product is assumed to be a composite of these hydrates with constant mechanical properties, as described in Section 4. Clearly, the chemical changes occurring during hydration affect the mechanical properties of the constituents. The incorporation of such time-dependent changes is a subject of ongoing work on advancing the proposed model.

6. Conclusions

A strategy for linking key microstructure characteristics of cement paste to its macroscopic behaviour is proposed as a development of the site-bond model. The strategy considers the paste as a three-phase medium and incorporates: (1) the volume fraction and size distribution of anhydrous cement particles as length-scale determining features; and (2) the porosity and pore size distribution as failure determining features. Basic material properties are required to accomplish the model: (1) engineering-scale elastic constants for calibration of local elasticity; and (2) atomic scale surface energy for definition of local failure. The result is thus a technology for predicting macroscopic properties from meso-scale principles. The following conclusions can be drawn from the findings presented:

- Damage development in cement paste, consequently the observed stress–strain response and fracture energy, depends strongly on the loading mode – this has important implications for the use of experimentally derived constitutive behaviours in e.g. integrity assessment of structures with existing macroscopic defects.
- Uniaxial tension generates distribution of local failures that maintains the material response isotropic. More complex loading conditions result in damage-induced anisotropic response with apparent embrittlement under equal other conditions.
- Porosity affects strongly the mechanical properties and damage evolution. Higher porosity yields more brittle response under equal other conditions. Tensile strength–porosity relation of cement paste can be expressed using the linear Hasselmann's equation and is in a good agreement with experimental results.
- Pore size distribution has an additional effect on the damage evolution and macroscopic behaviour. Larger fractions of large pores yield more brittle response. This result is consistent with basic fracture theory.

The work provides new insights into the failure behaviour of cement paste. The proposed technology can be used for the prediction of changes in mechanical properties and toughness with cement aging, so far as the changes in the microstructure are known. The site-bond modelling strategy can be extended to investigate the fracture processes and damage evolution in mortar and concrete, as well as in a large class of other quasi-brittle materials. Further, the strategy allows for the incorporation of time-dependent effects in cement-based materials. These opportunities are subject of ongoing works.

Acknowledgments

The authors acknowledge the support from EPSRC via Grant EP/J019763/1, "QUBE: Quasi-Brittle fracture: a 3D experimentally-validated approach", and from BNFL for the Research Centre for Radwaste & Decommissioning. The authors also express their gratitude to Dr. Y. He (Wuhan University of Technology, China) for sharing X-ray micro-CT image data used in this work.

References

[1] Haecker CJ, Garboczi EJ, Bullard JW, Bohn RB, Sun Z, Shah SP, et al. Modeling the linear elastic properties of Portland cement paste. Cem Concr Res 2005;35:1948–60.
[2] Zhang M, Ye G, van Breugel K. Multiscale lattice Boltzmann-finite element modelling of chloride diffusivity in cementitious materials. Part I: Algorithm and implementation. Mech Res Commun http://dx.doi.org/10.1016/j.mechrescom.2013.09.002.
[3] Bentz DP. Modelling cement microstructure: pixels, particles and property prediction. Mater Struct 1998;32:189–95.
[4] van Breugel K. Simulation of hydration and formation of structure in hardening cement-based materials. PhD Thesis, Delft University and Technology, Delft, The Netherlands; 1991.
[5] Ye G. Experimental study and numerical simulation of the development of the microstructure and permeability of cementitious materials. PhD Thesis, Delft University and Technology, Delft, The Netherlands; 2003.
[6] Bishnoi S, Scrivener KL. Mic: a new platform for modeling the hydration of cements. Cem Concr Res 2009;39:266–74.
[7] Zhang M, He Y, Ye G, Lange DA, van Breugel K. Computational investigation on mass diffusivity in Portland cement paste based on X-ray computed microtomography (μCT) image. Constr Build Mater 2012;27:472–81.
[8] Schlangen E, van Mier JGM. Experimental and numerical analysis of micromechanism of fracture of cement based composite. Cem Concr Compos 1992;14(2):105–18.
[9] Bolander JE, Choi S, Duddukuri SR. Fracture of fiber-reinforced cement composites: effects of fiber dispersion. Inter J Fracture 2008;154(1):73–86.
[10] Chang CS, Wang TK, Sluys LJ, van Mier JGM. Fracture modelling using a micro-structural mechanics approach – I. Theory and formulation. Eng Fract Mech 2002;69:1941–58.
[11] Lilliu G, van Mier JGM. 3D lattice type fracture model for concrete. Eng Fract Mech 2003;70:927–41.
[12] Šmilauer V, Bittnar Z. Microstructure-based micromechanical prediction of elastic properties in hydrating cement paste. Cem Concr Res 2006;36:1708–18.
[13] Yip M, Li Z, Liao B, Bolander JE. Irregular lattice models of fracture of multiphase particulate materials. Int J Fracture 2006;140:113–24.
[14] Bernard F, Kamali-Bernard S, Prince W. 3D multi-scale modelling of mechanical behaviour of sound and leached mortar. Cem Concr Res 2008;38:449–58.
[15] Man H. Analysis of 3D scale and size effects in numerical concrete. PhD Thesis, ETH Zürich, Switzerland; 2010.
[16] Grassl P, Jirasek M. Meso-scale approach to modelling the fracture process zone of concrete subjected to uniaxial tension. Int J Solids Struct 2010;47:957–68.
[17] Zheng J, Zhou X, Shao L, Jin X. Simple three-step analytical scheme for prediction of elastic moduli of hardened cement paste. J Mater Civil Eng 2010;22(1):1191–4.
[18] Pichler B, Hellmich C. Upscaling quasi-brittle strength of cement paste and mortar: a multi-scale engineering mechanics model. Cem Concr Res 2011;41:467–76.
[19] Qian Z. Multiscale modeling of fracture processes in cementitious materials. PhD Thesis, Delft University and Technology, Delft, The Netherlands; 2012.

[20] Jivkov AP, Engelberg DL, Stein R, Petkovski M. Pore space and brittle damage evolution in concrete. Eng Fract Mech 2013;110:378–95.
[21] Jivkov AP, Yates JR. Elastic behaviour of a regular lattice for meso-scale modelling of solids. Int J Solids Struct 2012;79:3089–99.
[22] Jivkov AP, Gunther M, Travis KP. Site-bond modelling of porous quasi-brittle media. Mineral Mag 2012;76:2969–74.
[23] Jivkov AP. Structure of micro-crack population and damage evolution in quasi-brittle media. Theor Appl Fract Mech 2014; http://dx.doi.org/10.1016/j.tafmec.2014.04.003, [in press].
[24] Zhang M, Morrison CN, Jivkov AP. A meso-scale site-bond model for elasticity: theory and calibration. Mater Res Innov 2014;18(S2):982–6.
[25] Zhao S, Zhao G. Implementation of a high order lattice spring model for elasticity. Int J Solids Struct 2012;49:2568–81.
[26] Bernard O, Ulm FJ, Lemarchand E. A multiscale micromechanics-hydration model for the early-age elastic properties of cement-based materials. Cem Concr Res 2003;33:1293–309.
[27] Djouani F, Chehimi MM, Benzarti K. Interactions of fully formulated epoxy with model cement hydrates. J Adhes Sci Technol 2013;27(5–6):469–89.
[28] Röβler M, Odler I. Investigations on the relationship between porosity, structure and strength of hydrated Portland cement pastes I. Effect of porosity. Cem Concr Res 1985;15:320–30.
[29] Chen X, Wu S, Zhou J. Influence of porosity on compressive and tensile strength of cement mortar. Constr Build Mater 2013;40:869–74.
[30] Balshin MY. Relation of mechanical properties of powder metals and their porosity and the ultimate properties of porous-metal ceramic materials. Dokl Askd Nauk SSSR 1949;67(67):831–4.
[31] Ryshkevitch R. Compression strength of porous sintered alumina and zirconia. J Am Ceram Soc 1953;36:65–8.
[32] Hasselman DPH. Griffith flaws and the effect of porosity on tensile strength of brittle ceramics. J Am Ceram Soc 1969;52:457.
[33] Schiller KK. Strength of porous materials. Cem. Concr. Res. 1971;1:419–22.